PHYSICAL REVIEW B **96**, 115311 (2017)

Theoretical and experimental investigation of the atomic and electronic structures at the $4H$-SiC(0001)/SiO$_2$ interface

Tomoya Ono[*]
Center for Computational Sciences, University of Tsukuba, Tsukuba, Ibaraki 305-8577, Japan
and JST-PRESTO, Kawaguchi, Saitama 332-0012, Japan

Christopher James Kirkham[†]
Center for Computational Sciences, University of Tsukuba, Tsukuba, Ibaraki 305-8577, Japan

Shoichiro Saito
Nitto Denko Corporation, Ibaraki, Osaka 567-8680, Japan

Yoshifumi Oshima
School of Materials Science, Japan Advanced Institute of Science and Technology, Nomi, Ishikawa, 923-1292, Japan

(Received 25 April 2017; revised manuscript received 11 August 2017; published 28 September 2017)

Density functional theory calculations are carried out to investigate the atomic and electronic structures of the $4H$-SiC(0001)/SiO$_2$ interface. We find two characteristic interface atomic structures in scanning transmission electron microscopy images: One is an interface in which the density of atoms at the first interfacial SiC bilayer is greater than that in the SiC substrate, while the other is an interface where the density of atoms at the first interfacial SiC bilayer is lower. Density functional theory calculations reveal that the difference in the scanning transmission electron microscopy images is a reflection of the atomic structures of these two interfaces. In addition, it has been reported that the floating states, which appear at the conduction band edge of a $4H$-SiC(0001)/SiO$_2$ interface, affect the electronic structure of the interface and cause marked scattering of the electrons flowing along the interface [S. Iwase, C. J. Kirkham, and T. Ono, Phys. Rev. B **95**, 041302(R) (2017)]. Interestingly, we find that the floating states do not appear at the conduction band edge of one of the two interfaces. These results provide physical insights into understanding and controlling the electronic structure and carrier mobility of electronic devices using wide-band-gap semiconductors.

DOI: 10.1103/PhysRevB.96.115311

I. INTRODUCTION

SiC is a technologically important material for future electronic devices where it can replace Si under extreme temperatures and voltages. SiC consists of hundreds of polymorphs (e.g., 3C, 4H, and 6H), with $4H$-SiC the most commonly used in actual devices, which can be grown as single-polymorph wafers [1]. An advantage of SiC over other wide-band-gap semiconductors is that, similarly to Si, its native oxide is SiO$_2$, making it ideal for metal-oxide-semiconductor field-effect transistors (MOSFETs). However, the carrier mobility of the SiC/SiO$_2$ interface is poor compared with that of bulk SiC [2]. This reduction in the carrier mobility is attributed to the high density of defects formed at the interface during thermal oxidation [3]. The atomic structure of SiC and SiO$_2$ at the interface affects its electronic properties as well as the possible types of defect. Thus, understanding the structure of both sides of the interface is important for improving the carrier mobility of SiC-MOSFETs.

Different interface atomic structures result in different electronic properties at the interface, such as band offsets and the position of defect states. Therefore, it is important to set up correct computational models when conducting theoretical investigations into the origins of the low carrier mobility of SiC-MOSFETs. Considerable experimental effort has been devoted to revealing the interface atomic structure [4]. High-resolution scanning transmission electron microscopy (STEM) observations indicated the existence of transition layers of nm-order thickness with an extremely high excess carbon concentration of approximately 20% beneath a SiC/SiO$_2$ interface, on the bulk SiC side [5–7]. However, later studies using x-ray photoelectron spectroscopy [8], medium-energy ion scattering [9], electron energy loss spectroscopy [10], and STEM [11] have raised doubts about the existence of these transition layers. Although the consensus is that transition layers with many excess carbon atoms are absent at the interface, to the best of our knowledge, the interface atomic structure of the SiC/SiO$_2$ interface has not been characterized completely by combined experimental and theoretical studies so far.

In this study, we perform density functional theory (DFT) [12] calculations to identify the SiO$_2$ polymorph directly at a $4H$-SiC(0001)/SiO$_2$ interface. For a Si/SiO$_2$ interface, in some cases, a crystalline phase of SiO$_2$ can be observed up to ∼10 Å from the interface [13–16], although SiO$_2$ is amorphous far from the interface [5–7,11]. Experimental STEM images of the interface reveals two configurations, where the atomic density of the interface differs in the interfacial atomic layer compared to the SiC substrate. One has a higher density of atoms than the substrate while the other has a lower density. A comparison

---

[*] ono@ccs.tsukuba.ac.jp

[†] Present address: Center for Materials Research by Information Integration, National Institute for Materials Science (NIMS), Tsukuba, Ibaraki, 305-0044, Japan.

between the STEM images and the atomic structures obtained by DFT calculations reveals that in the denser configuration, one of the four bonds of the Si atoms in the first interfacial Si layer of the SiO_2 region forms a bridge to the Si atoms in the first interfacial SiC bilayer of the SiC substrate via an O atom. In the sparser configuration, three bonds of the Si atoms in the first interfacial Si layer of the SiO_2 region are connected to the Si atoms in the first interfacial SiC bilayer of the SiC substrate. Hereafter, we refer to the former and latter configurations as one-bridging-bond and three-bridging-bond structures, respectively. It is also found that the SiO_2 immediately above the interface is similar to the β-tridymite or β-cristobalite phase in both the one-bridging-bond and three-bridging-bond structures. Moreover, in a previous study, we reported that the existence of the floating states lying at the conduction band edge (CBE) of the three-bridging-bond structure degrades the transmission probability of the conducting electrons [17,18] by first-principles electron-transport calculation [19–21]. Interestingly, it is found that the floating states do not appear at the CBE of the one-bridging-bond structure, and the absence of the floating states is explained by the strong electronegativity of O atoms at the interface. These results imply that the transmission probability of the conducting electrons in SiC/SiO_2 interface can be improved by controlling the electronegativity of the interface atoms.

II. METHODS OF STEM OBSERVATION

To characterize the interface atomic structure, a single-crystalline, nitrogen-doped, n-type (0001) Si-face 4H-SiC wafer manufactured by Cree Research is employed. A 4H-SiC(0001)/SiO_2 structure fabricated by the standard device fabrication process of dry oxidation and post-oxidation NO annealing of the SiC wafer is analyzed by high-resolution STEM. Details of the sample preparation and the oxidation process for the 4H-SiC(0001)/SiO_2 structure will be given elsewhere. The cross-sectional STEM specimen is prepared by a "sandwich" technique, in which two pieces of the sample with the same orientation are glued face-to-face using epoxy. After mechanically polishing the sandwich specimen, it is thinned by Ar^+ ion beam sputtering at a low incident angle. As much as possible of the damaged layer on the STEM sample surface is removed by ion milling with low accelerating voltage (no oxygen plasma cleaning is applied). Cross-sectional annular bright-field (ABF) images are taken by a spherical-aberration-corrected STEM at an accelerating voltage of 200 kV. The probe is converged with a semiangle of 24 mrad, within the range of which the electron beam is determined to be coherent by the Ronchigram. ABF images are obtained by collecting electrons scattered between semiangle of 12 and 24 mrad. The probe current is estimated to be 30 pA

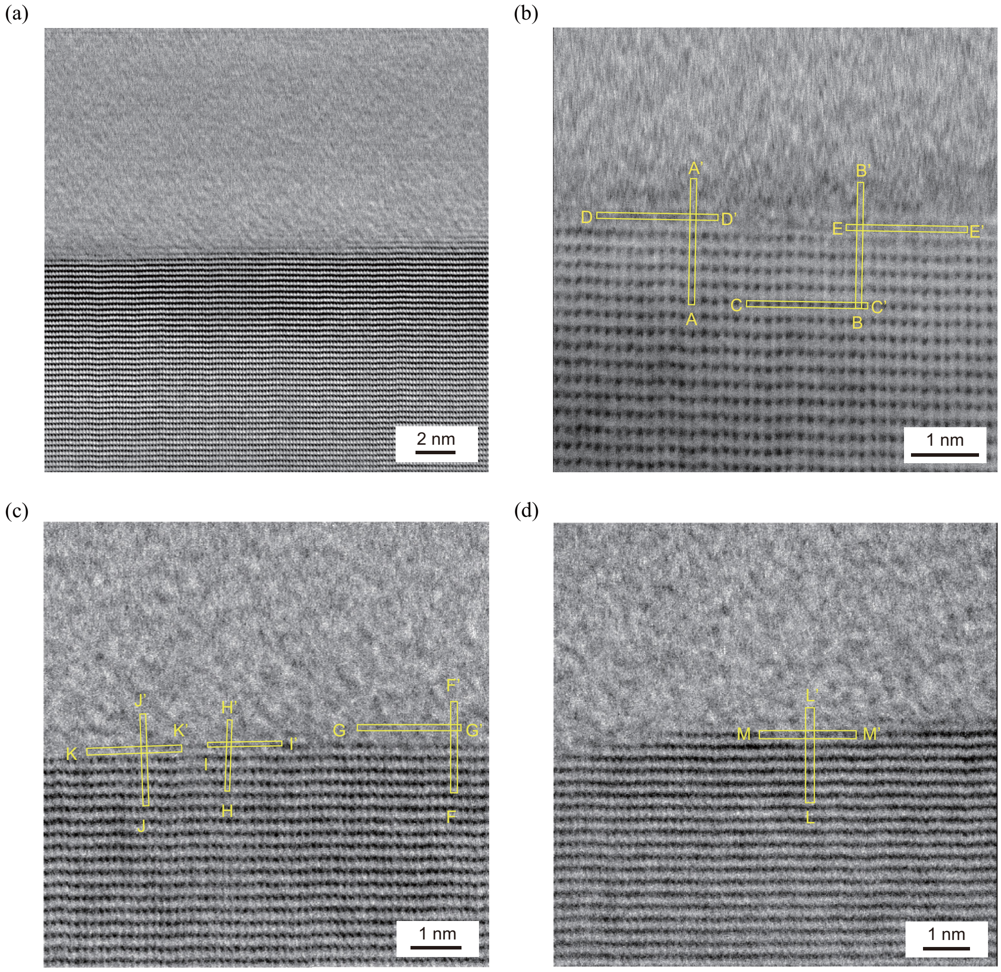

FIG. 1. (a) Low-magnification STEM image of the 4H-SiC(0001)/SiO_2 interface. (b)–(d) High-magnification STEM images. Dark spots correspond to the positions of atoms.

and the exposure time per pixel was 38 μs. Figure 1 shows ABF images of the interface between the 4H-SiC substrate and amorphous SiO_2 layers. The 4H-SiC substrate is viewed from the [1$\bar{1}$0] direction.

III. COMPUTATIONAL METHODS AND MODELS

DFT calculations are performed by the RSPACE code [19]. This code is based on a real-space finite-difference approach [22–26], which provides us with the ground-state atomic and electronic structures using a timesaving double-grid technique [24–26]. The electron-ion interactions are treated using the projector augmented-wave method [27] for the C, O, and Si atoms and using the norm-conserving pseudopotential [28] of Troullier and Martins [29,30] for the H atoms. The exchange-correlation functional is approximated by the local density approximation [31] of DFT. A coarse grid spacing of 0.16 Å is used for all the calculations.

Since most of the SiO_2 in the SiC(0001)/SiO_2 interface is amorphous according to the low-magnification STEM image shown in Fig. 1, it is not straightforward to characterize the interface atomic structure. Here, we assume atomic structures that can exist locally at the SiC(0001)/SiO_2 interface. Rather than construct and test interfaces for every single polymorph, we screen potential candidates on the basis of two criteria, following the case of the Si/SiO_2 interface [32]: lattice mismatch and the termination of dangling bonds (DBs) at the interface. Candidates with small lattice mismatches and where all DBs can be terminated are considered for further investigation and the other candidates are discarded. Table I shows the lattice mismatch between the SiC(0001) surface and SiO_2 polymorphs that satisfy the above criteria. The interface atomic structures are shown in Figs. 2(a)–2(d), in which the SiC(0001) surface is attached to α-quartz, α-cristobalite, β-tridymite, and β-tridymite, respectively. Note that the atomic configurations in the vicinity of the interface in Figs. 2(c) and 2(d) are the same when β-cristobalite is attached to the substrate, because the difference between the β-tridymite and β-cristobalite structures is the stacking along the direction perpendicular to the interface after the third interfacial Si layer of the SiO_2 region (ISiL). In Fig. 2(c), one of the four bonds of the Si atom in the first ISiL is connected to the Si atom in the first interfacial SiC bilayer of the SiC substrate (ISiCBL) via an O atom, and the other bonds are connected to the Si atoms in the SiO_2 region via O atoms, referred to as the one-bridging-bond structure. On the other hand, in Fig. 2(d), three bonds of the Si atoms in the first ISiL form bridges between the SiO_2 and the SiC substrate, referred to as the three-bridging-bond structure. In addition to these four structures, the interface atomic structure proposed by Knaup *et al.* [33], which is shown in Fig. 2(e), is also examined. Hereafter, we refer to the models depicted in Figs. 2(a), 2(b) and 2(e) as models the α-quartz, α-cristobalite, and two-bridging-bond structures, respectively.

Furthermore, it is noteworthy that there are two types of SiC(0001) surface orientation, the h and k types [34]. According to atomic force microscope observation of the surface, the terrace length of the h-type surface is longer than that of the k-type surface [35,36], which is explained by the difference in the total energies of the two interface types [37]. According to the low-magnification STEM image shown in Fig. 1(a), the SiC(0001) face has single layer steps, indicating that both interface types exist at the 4H-SiC(0001)/SiO_2 interface. Therefore, we examine the atomic and electronic structures for both interface types.

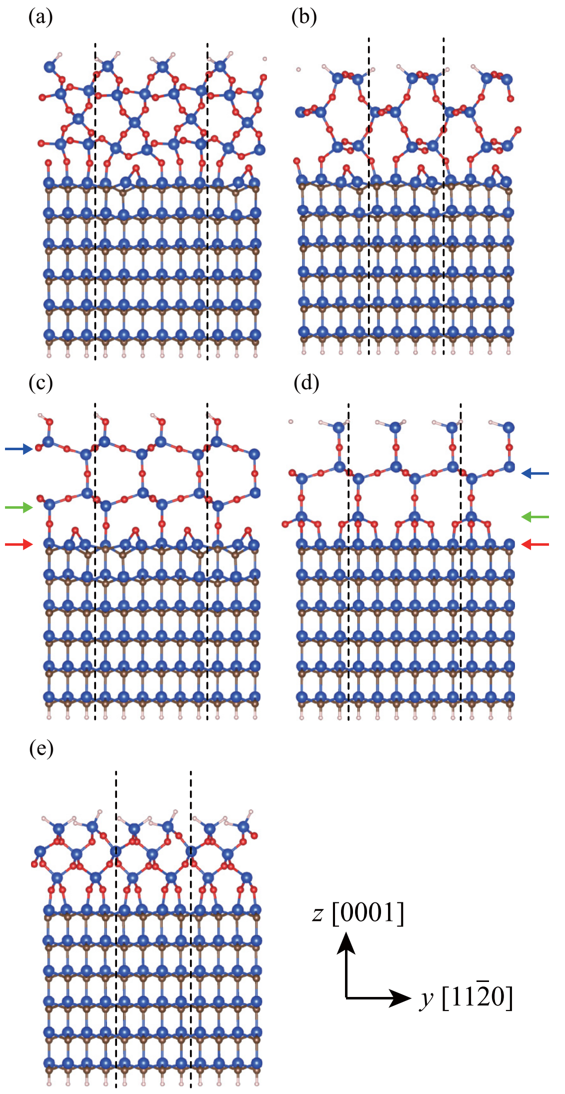

FIG. 2. Schematic image of interface atomic structures. (a)–(d) are models in which the SiC(0001) surface is attached to α-quartz, α-cristobalite, β-tridymite, and β-tridymite, respectively. Dashed lines indicate the boundary of the calculation supercell. In (c), one of the four bonds of the Si atom in the first interfacial Si layer of the SiO_2 region is connected to the Si atom in the first interfacial SiC bilayer of the SiC substrate via an O atom, and the other bonds are connected to the Si atoms in the SiO_2 region via O atoms. On the other hand, in (d), three bonds of the Si atoms in the first interfacial Si layer of the SiO_2 region form bridges between SiO_2 and SiC(0001). (e) Interface atomic structure proposed in Ref. [33]. White, red, gray, and blue balls are H, O, C, and Si atoms, respectively. The red, blue, and green arrows in (c) and (d) indicate the positions of the atomic layers of the first interfacial SiC bilayer of the SiC substrate, the first interfacial Si layer of the SiO_2 region, and the second interfacial Si layer, respectively.

The [1$\bar{1}$00], [11$\bar{2}$0], and [0001] directions are set to x, y, and z, respectively. The lateral lengths of the supercell are

TABLE I. Lattice mismatch between SiO_2 polymorphs and SiC(0001) substrate. Mismatches are calculated using experimental lattice parameters and are considered along SiC planes.

		$[1\bar{1}00]$ direction		$[11\bar{2}0]$ direction	
Polymorph	Crystal face	Crystal axis	Mismatch (%)	Crystal axis	Mismatch (%)
α-quartz SiO_2	$(1\bar{1}00)$	[0001]	+1.5	$[11\bar{2}0]$	+6.6
α-cristobalite SiO_2	(010)	[100]	−7.4	[001]	+11.4
β-tridymite SiO_2	(0001)	$[1\bar{1}00]$	−5.2	$[11\bar{2}0]$	−5.2
β-cristobalite SiO_2	(111)	$[1\bar{1}0]$	−5.2	$[11\bar{2}]$	−5.2

chosen to be $\sqrt{3}a$ and $3a$ ($2a$) along the $[1\bar{1}00]$ and $[11\bar{2}0]$ directions of the 4H-SiC(0001) surface, respectively, for the α-quartz, one-bridging-bond, and three-bridging-bond structures (α-cristobalite and two-bridging-bond structures), where $a(=3.08$ Å) is the experimental lattice constant of bulk 4H-SiC. The SiC substrate contains six SiC bilayers along the [0001] direction. The dangling bonds of the bottom SiC bilayer and the top SiO_2 layer are terminated by H atoms. The periodic boundary condition is applied to all directions and a sufficiently thick vacuum region of ∼12 Å is inserted. Integration over the Brillouin zone is carried out using a 2×2 (2×3) $\boldsymbol{k}$-point mesh for the α-quartz, one-bridging-bond, and three-bridging-bond structures (α-cristobalite and two-bridging-bond structures). We implement structural optimization until all the force components decrease to below 0.05 eV/Å, while the atomic coordinates of the SiC bilayer in the bottom layer and the H atoms terminating C dangling bonds are fixed during the structural optimization.

IV. RESULTS AND DISCUSSION

Figure 3 shows cross-sectional intensity profiles along the bars indicated in Fig. 1(b). The intensity profiles are averaged along the direction perpendicular to the profile as indicated by the width of bars in Fig. 1(b). There are two characteristic features in the image: In the profile along A-A’, the interlayer distance at the interface increases to 1.3–1.4 times that in the SiC substrate and the signal from the atomic layer becomes stronger before the increase in interlayer distance. The lattice distance along D-D’ is three times that along C-C’, indicating that line D-D’ is in the SiO_2 region. By comparison, in the profile along B-B’, the signal weakens before the interlayer spacing increases and the lattice distance along E-E’ is three times that along C-C’. These characteristic features can also be observed in other STEM images, as shown in Fig. 4. These results indicate that the atomic structure of the interface along A-A’ and B-B’ are different.

Table II lists the calculated interlayer spacings along the [0001] direction determined on the basis of the lateral spacing between Si atoms in neighboring layers, either within the SiC substrate and SiO_2 region or between two Si layers of the SiO_2 region. The interlayer spacing is insensitive to the orientation of the SiC substrate, i.e., the h and k types, at the interface. In addition, the interlayer spacing of the SiC substrate remains constant at 2.5 Å regardless of the SiO_2 polymorph. The one-bridging-bond structure shows the largest increase in interlayer spacing between the first ISiCBL and the first ISiL, by a factor of about 1.4–1.5, which is in rough agreement with the experimental results. The atomic layer spacing along the $[11\bar{2}0]$ direction of the SiC substrate in the first ISiL is three times that in the SiC substrate. In addition, the density of atoms in the first ISiCBL is greater than that in the SiC substrate, corresponding to the slight increase in the signal at the first ISiCBL in Fig. 3(a). Overall, the interface atomic structure of the one-bridging-bond structure

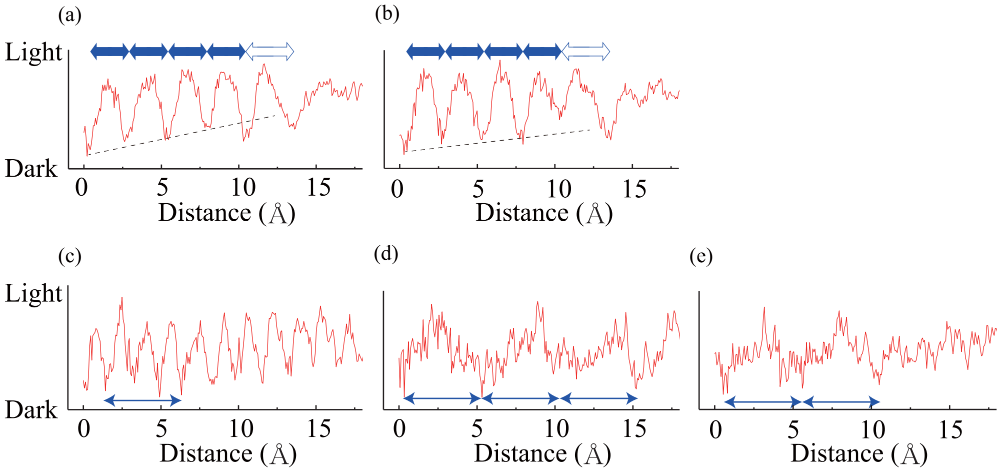

FIG. 3. Cross-sectional plots of STEM images along (a) A-A’, (b) B-B’, (c) C-C’, (d) D-D’, and (e) E-E’, as indicated in Fig. 1. The plots are averaged within the direction perpendicular to the plot line. In (a) and (b), the filled arrows indicate lengths equal to the interlayer spacings of bulk SiC while the open arrows are lengths exceeding that of the bulk. For clarity of the density of atoms, the dashed slopes are plotted in (a) and (b). In (c), (d), and (e), the arrows correspond to three times the interlayer spacings of bulk SiC.

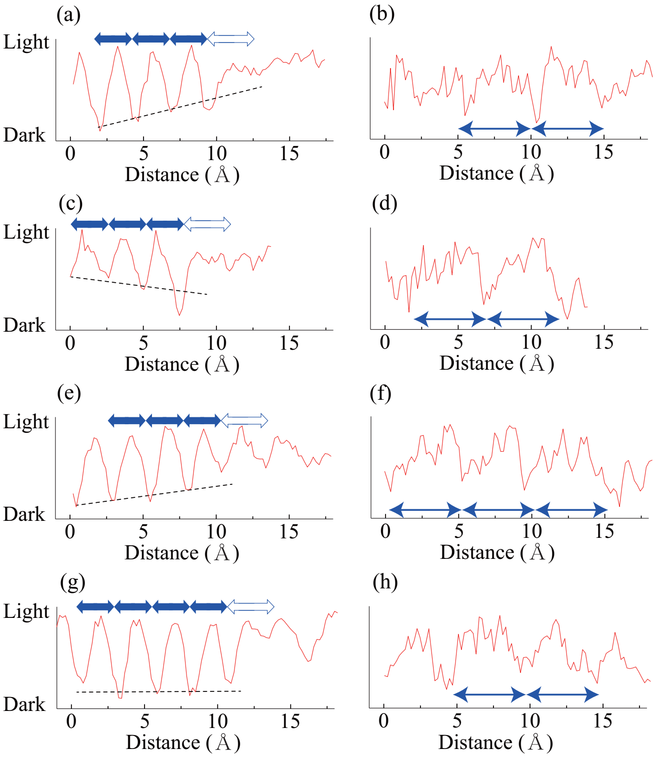

FIG. 4. Cross-sectional plots of STEM images along (a) F-F', (b) G-G', (c) H-H', (d) I-I', (e) J-J', (f) K-K', (g) L-L', and (h) M-M', as indicated in Fig. 1. The meanings of symbols are the same as those in Fig. 3. (a), (b), (c), and (d) correspond to the region of one-bridging-bond structure, while (d), (e), (f), and (g) are the region of three-bridging-bond structure.

corresponds well to the A-A' region. By comparison, the three-bridging-bond structure shows a significant increase in the interlayer spacing between the first and second ISiLs, while the interlayer spacing between the first ISiCBL and the first ISiL remains approximately the same as the SiC substrate. The atomic layer spacing along the $[11\bar{2}0]$ direction in the second ISiL is three times that in the SiC substrate. Moreover, the density of atoms in the first ISiL is lower than that in the SiC substrate, corresponding to the decrease in the signal before the increase in the interlayer spacing in B-B' [see Fig. 3(b)].

TABLE II. Interlayer spacing along the direction perpendicular to the interface. Si atoms within a region of 1 Å along the perpendicular direction are considered to be in the same layer. Average spacings between atomic layers are listed. Ratios to the interlayer distance in the SiC(0001) substrate are in parenthesis.

	Spacing (Å)	
Structure	1st ISiCBL-1st ISiL	1st ISiL-2nd ISiL
α-quartz str.	2.68 (1.07)	2.13 (0.85)
α-cristobalite str.	2.61 (1.04)	2.83 (1.13)
one-bridging-bond str.	3.70 (1.48)	4.22 (1.69)
three-bridging-bond str.	2.23 (0.89)	3.64 (1.46)
two-bridging-bond str.	2.62 (1.05)	2.04 (0.82)

TABLE III. Number of atoms in supercell, N^{thick} and N^{thin}, number of SiO$_2$ molecular unit, $N^{\text{thick}}_{SiO_2}$ and $N^{\text{thin}}_{SiO_2}$, number of excess O atoms, N_O, and formation energies per 1 × 1 region, E_{form}.

Structure	N^{thick}	N^{thin}	$N^{\text{thick}}_{SiO_2}$	$N^{\text{thin}}_{SiO_2}$	N_O	E_{form} (eV)
α-quartz str.	210	192	16	10	6	+0.44
α-cristobalite str.	132	120	8	4	4	+1.43
one-bridging-bond str.	186	174	8	4	6	+1.73
three-bridging-bond str.	186	174	8	4	6	0.00
two-bridging-bond str.	138	132	10	8	4	+3.31

None of the other computational models show a clear increase in the interlayer spacing from the SiC region at the interface.

We also examine the formation energy of the interface by employing models in which SiO$_2$ polymorphs are sandwiched between two $4H$-SiC(0001) substrates. The formation energy per 1 × 1 region, E_{form}, is calculated by varying the thickness of the SiO$_2$ polymorphs:

$$E_{\text{form}} = E^{\text{thin}} - \mu_{SiO_2} N^{\text{thin}}_{SiO_2} - \mu_O N_O, \quad (1)$$

$$\mu_{SiO_2} = (E^{\text{thick}} - E^{\text{thin}}) / \left(N^{\text{thick}}_{SiO_2} - N^{\text{thin}}_{SiO_2}\right), \quad (2)$$

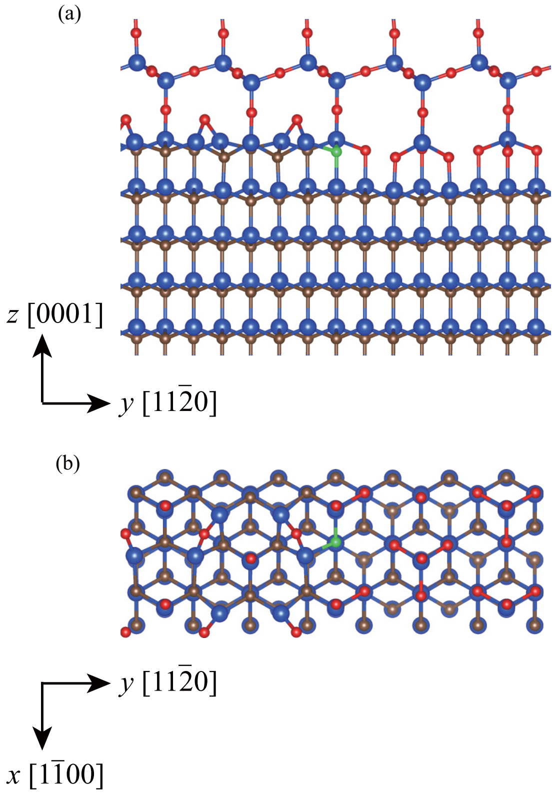

FIG. 5. Schematic images of combination of one-bridging-bond structure and three-bridging-bond structure. (a) Front view and (b) cross-sectional top view. Left is the one-bridging-bond structure side and right is the three-bridging-bond structure side. In the cross-sectional top view, the atoms above the first ISiL of the one-bridging-bond structure are removed for clarity. Red, gray, blue, and green balls are O, C, Si, and N atoms, respectively.

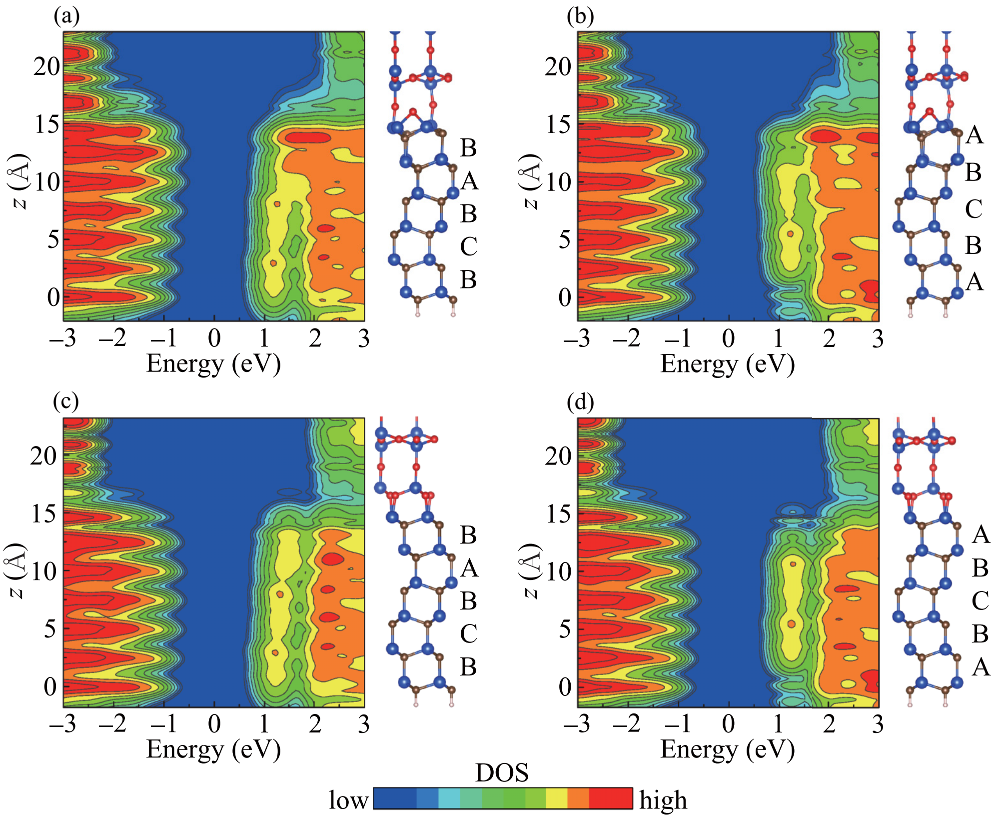

FIG. 6. Distributions of DOS integrated over a plane parallel to the interface as functions of energy relative to the Fermi energy. (a) One-bridging-bond structure in Fig. 2 with h-type $4H$-SiC(0001), (b) one-bridging-bond structure with k-type $4H$-SiC(0001), (c) three-bridging-bond structure with h-type $4H$-SiC(0001), and (d) three-bridging-bond structure with k-type $4H$-SiC(0001). Zero energy is chosen as the Fermi energy. Each contour represents twice or half the density of the adjacent contours and the lowest contour is 6.94×10^{-6} electron/eV/Å. The vertical axis is the height of the model. For clarity, structural models are provided to the right of each distribution.

where $E^{\mathrm{thin}}(E^{\mathrm{thick}})$ is the total energy of the thin (thick) SiO_2 model, $N^{\mathrm{thin}}_{SiO_2}(N^{\mathrm{thick}}_{SiO_2})$ is the number of SiO_2 molecular units in the thin (thick) model, μ_O is half the total energy of an O_2 molecule, and N_O is the number of excess O atoms. The contribution of μ_O to E_{form} is canceled when the formation energies are compared among the five models. Table III shows the numbers of atoms in the models and the calculated formation energies. It is found that the formation energy of the three-bridging-bond structure is the lowest. Indeed, the cross-sectional plots similar to Figs. 3(b) and 3(e) are frequently observed in other STEM images. On the other hand, the formation energy of the one-bridging-bond structure is the fourth lowest. Since the SiO_2 polymorph in the one-bridging-bond structure is the same with that in the three-bridging-bond structure, the existence of the one-bridging-bond structure is relevant to the three-bridging-bond structure. Figure 5 shows the combination of the one-bridging-bond and three-bridging-bond structures, in which no dangling bonds exist and no defect states appear in the band gap of SiC. Therefore, we can conclude that structures corresponding to the one-bridging-bond and three-bridging-bond structures are formed at part of the SiC(0001)/SiO_2 interface.

We next study the relationship between the atomic configuration and electronic structure at the interface. Figure 6 shows the distribution of the density of states (DOS) for the interface atomic structures for the one-bridging-bond and three-bridging-bond structures. The DOS is calculated as

$$\rho(z,E) = \sum_{i,k} \int |\Psi_{i,k}(x,y,z)|^2 \mathrm{d}x\mathrm{d}y \times N \mathrm{e}^{-\alpha(E-\varepsilon_{i,k})^2}, \qquad (3)$$

where $\varepsilon_{i,k}$ are the eigenvalues of the wave function, with indexes i and k denoting the eigenstate and the k-point respectively. $N(=2\sqrt{\frac{\pi}{\alpha}})$ is the normalization factor, where α is the smearing factor, here set to 13.5 eV^{-2}. The characteristic property of SiC is the existence of the floating states at the CBE, distributed in the interlayer region of the SiC bilayers [38,39]. In the DOS, several oval-like features appear at the CBE in the interlayer region, the location of which changes with the interface type. In the previous study using the three-bridging-bond structure, we concluded that the SiC/β-tridymite SiO_2 interface has one of these oval-like features at the first ISiCBL in the case of the h type, whereas they do not appear until the second ISiCBL in the case of the k type as shown in Figs. 6(c) and 6(d) [17]. This behavior at the CBE is not observed in the case of the Si/SiO_2 interface [40,41]. In addition, first-principles electron-transport calculations using nonequilibrium Green's function method revealed [19–21] that floating states for the three-bridging-bond structure with the h type interface causes carrier scattering at the $4H$-SiC(0001)/SiO_2 interface [18]. On the other hand, the one-bridging-bond structure shows different floating state behavior near the interface as shown in Figs. 6(a) and 6(b). For k type, the first floating states appear from the second ISiCBL, similar to in the three-bridging-bond structure. However, in contrast to the three-bridging-bond structure, for h type floating states do not appear at the CBE from the first ISiCBL. Since O atoms bridging the surface Si atoms exist in the vicinity of the first ISiCBL, the energy of the floating states is shifted upward owing to the strong electronegativity of the O atoms. This behavior of CBE states is significantly different from the Si/SiO_2 interface, where DFT calculations have reported that the electronic structure of the Si substrate is insensitive to the atomic configuration of the SiO_2 [42]. Although it is expected that several types of atomic structures appear at the $4H$-SiC(0001)/SiO_2 interface and that carrier scattering properties are significantly affected by the characteristic behavior of the floating states in some cases, this result implies that carrier scattering due to the floating states can be suppressed by controlling the electronegativity of the interface atoms.

V. CONCLUSIONS

The atomic structures of a crystalline phase that appear at part of the $4H$-SiC(0001)/SiO_2 interface are investigated by DFT calculations and STEM. Experimental ABF images reveal two configurations, in which the density of atoms in the atomic layer at the interface is either higher or lower than that in the SiC substrate. Comparing the ABF images with the atomic structures obtained from DFT calculations, we found that the higher configuration corresponds to the one-bridging-bond structure shown in Fig. 2(c), while the lower configuration is the three-bridging-bond structure shown in Fig. 2(d). In addition, it has been reported that, in the case of the three-bridging-bond structure, the floating states lying just beneath the interface causes scattering of the electrons flowing along the interface [17,18] We found that the floating states do not appear directly beneath the interface in the case of the one-bridging-bond structure. This will aid future work in determining the causes of the low carrier mobility of SiC-MOSFETs.

ACKNOWLEDGMENTS

This research was partially supported by MEXT as a social and scientific priority issue (creation of new functional devices and high-performance materials to support next-generation industries) to be tackled by using post-K computer, JSPS KAKENHI Grant No. JP16H03865, and JST PRESTO Grant No. JPMJPR13C3. The numerical calculations were carried out using the computer facilities of the Institute for Solid State Physics at the University of Tokyo, the Center for Computational Sciences at University of Tsukuba, and the K computer provided by the RIKEN Advanced Institute for Computational Science through the HPCI System Research project (Project ID: hp160228).

---

[1] T. Kimoto, Jpn. J. Appl. Phys. **54**, 040103 (2015).
[2] V. V. Afanas'ev, M. Bassler, G. Pensl, and M. Schulz, Phys. Status Solidi A **162**, 321 (1997).
[3] H. Yano, T. Kimoto, and H. Matsunami, Appl. Phys. Lett. **81**, 301 (2002).
[4] G. Liu, B. R. Tuttle, and S. Dhar, Appl. Phys. Rev. **2**, 021307 (2015).
[5] K. C. Chang, N. T. Nuhfer, L. M. Porter, and Q. Wahab, Appl. Phys. Lett. **77**, 2186 (2000).
[6] T. Zheleva, A. Lelis, G. Duscher, F. Liu, I. Levin, and M. Das, Appl. Phys. Lett. **93**, 022108 (2008).
[7] T. L. Biggerstaff, C. L. Reynolds, Jr., T. Zheleva, A. Lelis, D. Habersat, S. Haney, S.-H. Ryu, A. Agarwal, and G. Duscher, Appl. Phys. Lett. **95**, 032108 (2009).
[8] H. Watanabe, T. Hosoi, T. Kirino, Y. Kagei, Y. Uenishi, A. Chanthaphan, A. Yoshigoe, Y. Teraoka, and T. Shimura, Appl. Phys. Lett. **99**, 021907 (2011).
[9] X. Zhu, H. D. Lee, T. Feng, A. C. Ahyi, D. Mastrogiovanni, A. Wan, E. Garfunkel, J. R. Williams, T. Gustafsson, and L. C. Feldman, Appl. Phys. Lett. **97**, 071908 (2010).
[10] T. Hatakeyama, H. Matsuhata, T. Suzuki, T. Shinohe, and H. Okumura, Mater. Sci. Forum **679-680**, 330 (2011).
[11] J. A. Taillon, J. H. Yang, C. A. Ahyi, J. Rozen, J. R. Williams, L. C. Feldman, T. S. Zheleva, A. J. Lelis, and L. G. Salamanca-Riba, J. Appl. Phys. **113**, 044517 (2013).
[12] P. Hohenberg and W. Kohn, Phys. Rev. **136**, B864 (1964).
[13] T. Simura, H. Misaki, M. Umeno, I. Takahashi, and J. Harada, J. Cryst. Growth **166**, 786 (1996).
[14] I. Takahashi, T. Shimura, and J. Harada, J. Phys.: Condens. Matter **5**, 6525 (1993).
[15] A. Ourmazd, D. W. Taylor, J. A. Rentschler, and J. Bevk, Phys. Rev. Lett. **59**, 213 (1987).
[16] F. Rochet, M. Froment, C. D'Anterroches, H. Roulet, and G. Dufour, Philos. Mag. B **59**, 339 (1989).
[17] C. J. Kirkham and T. Ono, J. Phys. Soc. Jpn. **85**, 024701 (2016).
[18] S. Iwase, C. J. Kirkham, and T. Ono, Phys. Rev. B **95**, 041302(R) (2017).
[19] K. Hirose, T. Ono, Y. Fujimoto, and S. Tsukamoto, *First Principles Calculations in Real-Space Formalism, Electronic Configurations and Transport Properties of Nanostructures* (Imperial College, London, 2005).
[20] T. Ono, Y. Egami, and K. Hirose, Phys. Rev. B **86**, 195406 (2012).
[21] T. Ono and S. Tsukamoto, Phys. Rev. B **93**, 045421 (2016).
[22] J. R. Chelikowsky, N. Troullier, and Y. Saad, Phys. Rev. Lett. **72**, 1240 (1994).
[23] J. R. Chelikowsky, N. Troullier, K. Wu, and Y. Saad, Phys. Rev. B **50**, 11355 (1994).
[24] T. Ono and K. Hirose, Phys. Rev. Lett. **82**, 5016 (1999).
[25] T. Ono and K. Hirose, Phys. Rev. B **72**, 085115 (2005).
[26] T. Ono, M. Heide, N. Atodiresei, P. Baumeister, S. Tsukamoto, and S. Blügel, Phys. Rev. B **82**, 205115 (2010).
[27] P. E. Blöchl, Phys. Rev. B **50**, 17953 (1994).
[28] We used the norm-conserving pseudopotentials NCPS97 constructed by K. Kobayashi. See K. Kobayashi, Comput. Mater. Sci. **14**, 72 (1999).

[29] L. Kleinman and D. M. Bylander, Phys. Rev. Lett. **48**, 1425 (1982).
[30] N. Troullier and J. L. Martins, Phys. Rev. B **43**, 1993 (1991).
[31] S. H. Vosko, L. Wilk, and M. Nusair, Can. J. Phys. **58**, 1200 (1980).
[32] H. Kageshima and K. Shiraishi, Phys. Rev. Lett. **81**, 5936 (1998).
[33] J. M. Knaup, P. Deák, T. Frauenheim, A. Gali, Z. Hajnal, and W. J. Choyke, Phys. Rev. B **71**, 235321 (2005).
[34] H. Matsunami and T. Kimoto, Mater. Sci. Eng. **R20**, 125 (1997).
[35] K. Arima, H. Hata, J. Murata, T. Ishida, R. Okamoto, K. Yagi, Y. Sano, H. Murata, and K. Yamauchi, Appl. Phys. Lett. **90**, 202106 (2007).
[36] K. Arima, K. Endo, K. Yamauchi, K. Hirose, T. Ono, and Y. Sano, J. Phys.: Condens. Matter **23**, 394202 (2011).
[37] H. Hara, Y. Morikawa, Y. Sano, and K. Yamauchi, Phys. Rev. B **79**, 153306 (2009).
[38] Y. I. Matsushita, S. Furuya, and A. Oshiyama, Phys. Rev. Lett. **108**, 246404 (2012).
[39] Y. I. Matsushita and A. Oshiyama, Phys. Rev. Lett. **112**, 136403 (2014).
[40] T. Ono, Phys. Rev. B **79**, 195326 (2009).
[41] T. Ono and S. Saito, Appl. Phys. Express **4**, 021303 (2011).
[42] T. Yamasaki, C. Kaneta, T. Uchiyama, T. Uda, and K. Terakura, Phys. Rev. B **63**, 115314 (2001).